Full spectrum light driven photocatalytic in-situ epitaxy of one-unit-cell $Bi_2O_2CO_3$ layers on Bi_2O_4 nanocrystals for highly efficient photocatalysis and mechanism unveiling

Jun Li[a,1], Xiaoyong Wu[a,1], Zhen Wan[a], Hong Chen[b], Gaoke Zhang[a,*]

[a] *State Key Laboratory of Silicate Materials for Architectures, Hubei Key Laboratory of Mineral Resources Processing and Environment, Hubei Provincial Collaborative Innovation Center for High Efficient Utilization of Vanadium Resources, Wuhan University of Technology, 122 Luoshi Road, Wuhan, 430070, China*
[b] *SSRL, SLAC National Accelerator Laboratory Stanford University, Menlo Park, CA, 94025, USA*

ARTICLE INFO

ABSTRACT

In-situ epitaxial growth is a fascinating strategy to nicely couple two low dimensional semiconductors as highly efficient composite photocatalysts. Meanwhile, organic contaminants in the photocatalytic process are usually decomposed into greenhouse gas (CO_2) that can't be reused. Herein, we reported a green full spectrum light (UV, visible and NIR lights) induced epitaxial growth strategy to synthesize highly efficient $Bi_2O_4/Bi_2O_2CO_3$ heterostructure photocatalyst by reusing waste carbon source, in which one-unit-cell $Bi_2O_2CO_3$ layers (1.0 nm) in-situ grew on the surface of Bi_2O_4 nanocrystals during the photocatalytic degradation of rhodamine B (RhB) or phenol. More importantly, ^{13}C nuclear magnetic resonance (NMR) spectroscopy confirmed that the carbon element in $Bi_2O_2CO_3$ was from the photocatalytic degradation of organic contaminations. Furthermore, density functional theory (DFT) calculations confirm that the Bi_2O_4 nanocrystals with exposed {-101} facets have the larger percentage of undercoordinated Bi atoms, which provided favorable conditions for the in-situ epitaxy of $Bi_2O_2CO_3$ during the photocatalytic reaction. Additionally, the increased charge density near the Fermi level resulted in improved photoresponsivity of $Bi_2O_4/Bi_2O_2CO_3$ composite and the coalescence of Bi_2O_4 and $Bi_2O_2CO_3$ could favor the travel of photogenerated carriers from one to another owing to the close work functions for Bi_2O_4 (4.295 eV) and $Bi_2O_2CO_3$ (4.410 eV). As we expected, the $Bi_2O_4/Bi_2O_2CO_3$ composite presented higher photocatalytic activity for phenol and ciprofloxacin (CIP) degradation than pure Bi_2O_4 nanocrystals. The possible degradation pathway of CIP in aqueous solution and photocatalytic mechanism of $Bi_2O_4/Bi_2O_2CO_3$ composite were also proposed based on liquid chromatography mass spectrometer (LC–MS) analysis and experimental results. This work provides a green strategy for designing highly efficient photocatalysts.

1. Introduction

Low-dimensional (LD) semiconductor photocatalysts have attracted massive attention on account of their extraordinary properties and promising applications in photocatalytic fields [1–8]. Abundant visible light responsive two-dimensional (2D) Bi-containing photocatalysts have been studied due to their facile hole mobility and fantastic optical properties, benefiting from its filled Bi 6 s band of Bi^{3+} and empty 6 s band of Bi^{5+} [9–11] for photocatalytic degradation of organic contaminants, such as $Bi_{12}MnO_{20}$ [12], Bi_2WO_6 [13], BiOX (X = Cl, Br, I) [14,15], and so on. Although the reported 2D photocatalysts have revealed good photocatalytic activity, the efficiency of photocatalytic approach normally suffers from woeful charge transfer property and

slow interfacial kinetics for degradation of organic pollutants. Hence, abundant works have been performed to overcome these shortcomings, such as loading co-catalysts or fabricating type-II heterostructure photocatalysts with staggered band alignments [16–21]. Epitaxial growth as a perfect strategy by the vertical or lateral epitaxial growth of other nanomaterials on one LD materials, which can passivate the surface trap states for improving the separation efficiency of carriers, has drawn extensive attention [22–30]. Moreover, the fabricating of semiconductor heterostructures by epitaxial growth strategy can generate strong interface electric field by band-edge offset, which is different from the normal heterostructures. For example, 2D transition metal dichalcogenide (TMD) nanosheets (NSs) (i.e., MoS_2 and $MoSe_2$) are vertically grown along the longitudinal direction of one-dimensional

---

(1D) $Cu_{2-x}S$ nanowires (NWs) for facilitating the charge transfer between 2D TMD NSs and 1D NWs and thus enhance their photocatalytic activity due to the introduced strong interface electric field by band-edge offset [31]. The strategies for epitaxial growth are generally involved in chemical vapor deposition (CVD), electrochemical strategy, cation exchange, van der Waals epitaxy and so on [22,31–34]. Therefore, the development of low-cost, highly efficiency and green epitaxial growth way is still greatly promising.

Herein, we developed a green light-induced in-situ epitaxial strategy to synthesize $Bi_2O_4/Bi_2O_2CO_3$ heterostructure as a proof-of-concept, in which one-unit-cell $Bi_2O_2CO_3$ layers in-situ grew from the surface of Bi_2O_4 nanocrystals. Interestingly, the carbon source for the epitaxial growth of $Bi_2O_2CO_3$ was originated from the photocatalytic degradation of contaminants rather than adding extra carbon raw materials. This peculiar phenomenon was systematically studied and then confirmed by a series of characterization techniques. Therefore, the carbon species from contaminants degradation could be reused and then be applied in the photocatalytic field. Owing to the in situ epitaxial growth of $Bi_2O_2CO_3$ on Bi_2O_4, a strong interface contact and well-aligned band structures were perfectly formed, in this case, the photogenerated electrons in the conduct band (CB) of Bi_2O_4 could be rapidly injected into CB of ultrathin $Bi_2O_2CO_3$ nanosheets, achieving the efficient separation of electron-hole pairs and resulting in a photocurrent of 16 $\mu A\,cm^{-2}$, nearly 2 times higher than that of Bi_2O_4. As expected, $Bi_2O_4/Bi_2O_2CO_3$ composite exhibited higher property for photocatalytic degradation of phenol and CIP than pure Bi_2O_4 under the irradiation of visible light. This work developed a green in situ epitaxial growth method for the fabrication of well-matched highly efficient heterojunction photocatalysts.

2. Experimental section

2.1. Materials

Sodium bismuthate oxide ($NaBiO_3$) and sodium hydroxide (NaOH) were purchased from Alfa or Sinopharm Chemical Reagent Co., Ltd., Shanghai, China. All the reagents are analytical grade and used without further purification.

2.2. Photocatalyst preparation

2.2.1. Synthesis of Bi_2O_4 nanocrystals

The monoclinic Bi_2O_4 was synthesized by a facile solvothermal method. Generally, 10 mmol $NaBiO_3$ and 6 mmol NaOH were mixed into 60 mL of deionized water. And then, the mixtures were stirred for 1 h to make it homogeneous solution. After that, the suspensions were transformed into a 90 mL polyphenylene (PPL)-lined autoclave, which was sealed and heated at 180 °C for 6 h, and when the reaction temperature cooled to room temperature, the as-prepared samples were collected by centrifugation and washed five times by deionized water. At last, the as-prepared samples were dried at 80 °C for 4 h.

2.2.2. Synthesis of $Bi_2O_2CO_3$ nanosheets

4.85 g of $Bi(NO_3)_3 \cdot 5H_2O$ were dissolved in 10 mL of 1 mol L^{-1} HNO_3 aqueous solution and stirred for 30 min at room temperature to form a clear solution (denoted as solution A). In addition, 1.0 g of cetyltrimethylammonium bromide (CTAB) and 8.45 g of $Na_2CO_3 \cdot 10H_2O$ were added to 90 mL distilled water (denoted as solution B). Then, solution A was dropped into solution B with constant stirring. After 10 min of stirring, the resulting white precipitate was filtered, washed with distilled water and ethanol for three times and dried at 80 °C for 4 h.

2.2.3. Fabrication of $Bi_2O_4/Bi_2O_2CO_3$ composite

0.1 g Bi_2O_4 photocatalysts were added into 100 mL of RhB aqueous solution (10 mg L^{-1}) in a beaker. Then, the mixed suspensions were continuously stirred under 100 W LED lamp irradiation for 1–3 h. Finally, the suspensions were washed with distilled water for three times and dried at 80 °C for 4 h and denoted as $Bi_2O_4/Bi_2O_2CO_3$ (1 h), $Bi_2O_4/Bi_2O_2CO_3$ (2 h) and $Bi_2O_4/Bi_2O_2CO_3$ (3 h), respectively.

2.2.4. Fabrication of $Bi_2O_4/Bi_2O_2{}^{13}CO_3$ composite

0.1 g Bi_2O_4 photocatalysts were added into 100 mL of phenol aqueous solution (10 mg L^{-1}), which was marked by ^{13}C isotope in a beaker. Then, the mixed suspensions were continuously stirred under 100 W LED lamp irradiation for a 1, 2, 3 h. Finally, the suspensions were washed with deionized water for five times and dried at 80 °C for 4 h.

2.3. Characterization

The typical $Bi_2O_4/Bi_2O_2CO_3$ (2 h) was selected to study its physicochemical property in representative characterizations. The phase and crystallinity of the samples were determined by X-ray diffraction (XRD) analysis on a D/MAX-RB diffractometer and operated at 40 kV voltage and 50 mA current. The absorption edges of the as-prepared samples were tested by diffuse reflectance spectra (UV2550, Shimadzu Corporation, Kyoto, Japan). X-ray photoelectron spectra (XPS) was measured on a PHI Quantera system with a monochromatic Al Kα source. Photoluminescence (PL) measurements were performed on a fluorescence spectrophotometer (RF-5301 PC, Shimadzu, Japan) at room temperature. The morphology and microstructure of the samples were measured by scanning electron microscopy (SEM, JSM-5610LV), transmission electron microscopy (TEM) and high-resolution transmission electron microscopy (HRTEM) using a JEM 2100 F electron microscope, which was operated at an accelerating voltage of 200 kV. Decay curves of the as-prepared products were obtained on a FLS920 fluorescence lifetime spectrophotometer (Edinburgh Instruments, UK) with excitation at 325 nm and emission at 650 nm. Solid-state ^{13}C NMR experiments were performed on a Bruker Avance I-500 MHz spectrometer to detect the formation of $Bi_2O_2{}^{13}CO_3$ nanosheets. Agilent 6410 Liquid Chromatography Mass Spectrometer (LC–MS, USA) was employed to identify the degradation intermediates of ciprofloxacin (CIP) in aqueous solution by the as-prepared sample under visible light irradiation.

2.4. Photoelectrochemical measurement

The photoelectrochemical properties of the as-prepared samples were observed in a homemade three-electrode cell using a computer-controlled electrochemical workstation. Firstly, the as-prepared samples composites (75 mg) were suspended in absolute ethyl alcohol solution (1 mL), and then collodion (0.1 g) was added into the ethyl alcohol solution, finally, the suspension was magnetically stirring for 1 h until forming a homogeneous solution and Fluorine doped stannic oxide (FTO) electrode was cleaned by NaOH (1 mol L^{-1}) and H_2O_2 (30 wt%), and then washed by acetone and deionized water, next dried at room temperature. The above solution was dropped onto the FTO glass with settled area (2 cm × 3 cm). After the evaporation of solution in an ambient environment, the FTO glasses with photocatalysts were put into the oven at 60 °C for 8 h. The prepared pure Bi_2O_4 or $Bi_2O_4/Bi_2O_2CO_3$, a platinum sheet and a mercurous chloride electrode were used as working electrode, counter electrode, and reference electrode respectively. The 0.5 M Na_2SO_4 was chosen as the electrolyte.

2.5. The photocatalytic activity evaluation

For exploring the photocatalytic performance of the as-synthesized $Bi_2O_4/Bi_2O_2CO_3$ composite, the phenol was selected as the model to assess its photocatalytic performance under visible light irradiation. Typically, 0.1 g samples were added into 100 mL of phenol aqueous solution (10 mg L^{-1}). For eliminating the influence of the adsorption,

the mixed suspensions were continually stirred for 0.5 h in the dark. Moreover, the suspensions were irradiated with visible light which was supplied by a 100 W LED lamp with the wavelength of 420 nm. At set time for 30 min, the homogeneous suspensions were taken for 6 mL, centrifugalized, and then analyzed by employing a UV–vis spectrophotometer (UV751GD, China) at its maximum absorption wavelength of 270 nm.

2.6. Theoretical calculations

In order to study the electronic structure, surface energies and work functions of the samples, DFT (density functional theory) calculations have been carried out using the Vienna ab initio Simulation Package (VASP) code with the projector-augmented wave (PAW) scheme, we selected generalized gradient approximation (GGA) within the Perdew-Burke-Ernzerh (PBE) of exchange-correlation functional [35–37]. In the work, an energy cuts off 400 eV was used for the of Bi_2O_4 and $Bi_2O_2CO_3$. The lattice parameters of the Bi_2O_4 and $Bi_2O_2CO_3$ were a = 12.367 Å, b = 5.118 Å, c = 5.299 Å, and a = 3.865 Å, b = 3.862 Å, c = 13.675 Å, respectively. The $1 \times 2 \times 2$ and $3 \times 3 \times 1$ k-point meshes were used for pristine Bi_2O_4 and $Bi_2O_2CO_3$, separately. The {-100} facet, {-111} facet and {-110} facet of Bi_2O_4 were modeled with 2 nm thicknesses without fixing any layers from the crystal along [-111], [-110] and [-100] orientation, respectively. The vacuum separation between the slabs was set to be 15 Å. All the optimizations of atomic geometry were performed until all components of residual force were less than $0.02 \, eV \, Å^{-1}$. The iterative energy difference was less than 10^{-4} eV. The surface energy E_{surf} was defined as: [38]

$$E_{surf} = (E_{slab} - n \times E_{bulk})/(2 \times A)$$

where E_{slab}, E_{bulk}, n and A represent the total energy of the relaxed slab, the total energy of the bulk, the number of the bulk unit cells in the supercell and the surface area, respectively.

3. Results and discussion

The $Bi_2O_4/Bi_2O_2CO_3$ heterostructure was prepared via green photocatalytic strategy under light irradiation with different wavelengths and the carbon source of $Bi_2O_2CO_3$ was originated from the decomposition of organic pollutants in liquid phase. The TEM image of the $Bi_2O_4/Bi_2O_2CO_3$ (2 h) heterostructure in the inset of Fig. 1a shows that the transparent $Bi_2O_2CO_3$ layers were in-situ growth on the surface of Bi_2O_4. Subsequently, $Bi_2O_4/Bi_2O_2CO_3$ composites were obtained under different light irradiation time, their phase composition and morphology were attested by XRD (Fig. S1a) and SEM (Fig. S1b–f). The XRD patterns of the composites could be well indexed into the tetragonal phase of $Bi_2O_2CO_3$ (JCPDS No. 41-1448) and monoclinic phase of Bi_2O_4 (JCPDS No. 50-0864). With increasing irradiation time, the epitaxial growth of $Bi_2O_2CO_3$ was limited (Fig. S1). The HRTEM image in Fig. 1a depicts $Bi_2O_4/Bi_2O_2CO_3$ composite gained under visible light irradiation for 2 h. The evident heterojunction structure with a clear transition through their interface. The lattice fringe of (20-2) planes of Bi_2O_4 (0.275 nm) is very accordance with that (0.273 nm) of (110) plane of $Bi_2O_2CO_3$, confirming the well-matched lattice parameters between Bi_2O_4 and $Bi_2O_2CO_3$ ensure the epitaxial growth of $Bi_2O_2CO_3$ on Bi_2O_4 nanocrystals (Fig. S2) [24]. Moreover, the selected area electron diffraction (SAED) images of Bi_2O_4 and $Bi_2O_2CO_3$ verified that they possess [-101] and [001] orientations, respectively, indicating that the {-101} and {001} facets are the main exposed facet of Bi_2O_4 and $Bi_2O_2CO_3$, separately (Fig. 1b and c). The thickness of nearly transparent epitaxial grown $Bi_2O_2CO_3$ was detected by atomic force microscopy (AFM) (Fig. 1d and e). The thickness of these nanosheets is estimated to be about ~ 1.1 nm, which is consistent with that of one-unit-cell $Bi_2O_2CO_3$ slab along the c axis (Fig. 1f). Fig. 1g and h describe the schematic diagram of $Bi_2O_4/Bi_2O_2CO_3$ heterojunction and the pristine morphology of Bi_2O_4 nanocrystals with rod-like structure. The

achievement of the reusing carbon source from organic pollutants in the photocatalytic process and the $Bi_2O_4/Bi_2O_2CO_3$ composite is composed by Bi, C and O elements (Fig. 1i–l). The light sources with different wavelengths from UV to NIR light were used to study the epitaxial growth of $Bi_2O_2CO_3$ on the surface of Bi_2O_4 nanocrystals. The corresponding SEM images and XRD patterns prove the presence of $Bi_2O_2CO_3$ sheets (Fig. S3-4), and the generation of $Bi_2O_2CO_3$ apparently depends on the photocatalytic degradation of RhB in aqueous solution by Bi_2O_4 photocatalyst (Fig. S4-5).

For exploring the generality of our method, we further in situ synthesized $Bi_2O_4/Bi_2O_2CO_3$ heterostructures by replacing the RhB with colorless phenol. Fig. 2a–d show the typical TEM images of $Bi_2O_4/Bi_2O_2CO_3$ composite, in which one-unit-cell $Bi_2O_2CO_3$ layers in-situ grew from the surface of Bi_2O_4 nanocrystals (see XRD pattern in Fig. S6). The lattice fringes through the interface between Bi_2O_4 nanocrystals and one-unit-cell $Bi_2O_2CO_3$ layers can be detected in the HRTEM image of $Bi_2O_4/Bi_2O_2CO_3$ heterostructures, suggesting the epitaxial growth of 2D ultrathin $Bi_2O_2CO_3$ nanosheets on 1D Bi_2O_4 nanocrystals. The covalent bond connection property and well-matched lattice parameters obtained by in-situ grown ultrathin $Bi_2O_2CO_3$ nanosheets guarantee the epitaxial growth of abundant one-unit-cell $Bi_2O_2CO_3$ layers on 1D Bi_2O_4 nanocrystals, which is different from reported LD heterostructures [39].

To further identify the carbon source of $Bi_2O_2CO_3$ and elucidate the formation mechanism of $Bi_2O_4/Bi_2O_2CO_3$ composite, the solid-state ^{13}C NMR analysis of the obtained samples were performed [40]. The spectra mainly show four peaks with different intensities, which are behalf on the content. A comparison of solid-state ^{13}C NMR spectra of the photocatalytically oxidized phenol provides an insight into the possible degradation profile and the formation process of $Bi_2O_4/Bi_2O_2CO_3$ composite. For better analyzing the peaks, they could be grouped into three types: i) 123.3 ppm and 129.2 ppm, ii) 153.9 ppm and iii) 185 ppm. Fig. 2e shows the solid-state ^{13}C NMR spectra of Bi_2O_4 during visible light photocatalytic degradation of phenol and the peak with the highest intensity is observed at 129.2 ppm. The peaks located at the 123.3 ppm and 129.2 ppm are primarily attributed to phenyl ring arising from phenol. The existence of phenol in $Bi_2O_4/Bi_2O_2CO_3$ composite is mainly caused by the adsorption during the photocatalytic degradation of phenol. Compared to the dark reaction, the new peak intensity at 153.9 ppm could be ascribed to carbon structure of $Bi_2O_2CO_3$ and the peak intensity increased with increasing irradiation time, suggesting the $Bi_2O_2CO_3$ was in-situ growth on Bi_2O_4 nanocrystals [41]. The peak at 185.0 ppm could result from the intermediate products during photocatalytic degradation of phenol, such as HCOOH, CH_3COOH or other lower aliphatic carboxylic acids [42]. Fig. 2f reveals the solid-state ^{13}C NMR spectra of Bi_2O_4 exposed under the light irradiation with different wavelengths for photocatalytic degradation of phenol, indicating that the $Bi_2O_2CO_3$ was successfully in-situ growth on Bi_2O_4 nanocrystals.

Based on the above experimental results, the surface structure of Bi_2O_4 with different facets was further investigated by the DFT calculation to clarify the epitaxial growth mechanism. The representative relaxed atomic geometries of each slab were displayed in Fig. 3a–c. On the surface of {-100} facet, the Bi and O atoms on the top layer are undercoordinated: Bi atoms reveal 2-fold and 5-fold coordinated (Bi_{2c} and Bi_{5c}). On the surface {-111} facet, the Bi_{6c} atoms and Bi_{4c} on the top layer, the fully (6-fold/4-fold)-coordinated Bi_{6c} and Bi_{4c} atoms are present, because the Bi_2O_4 is the bismuth oxide with mixed valence states, its structure has two types of full coordination. On the {-101} facet, Bi_{3c} and Bi_{2c} co-exists in the structure, indicating beneficial atomic structure, on which the large percentage of undercoordinated Bi atoms (Bi_{3c} and Bi_{2c}) could act as the active reaction sites in the photocatalytic reaction. In addition, the surface energy (E_{surf}) of Bi_2O_4 was calculated to be 1.93, 1.5 and 3.10 J m^{-2} for {-100}, {-111} and {-101} facets, separately. Compared with {-100}, {-111} and {-101} facets, the highest surface energy of {-101} facet could be ascribed to the large
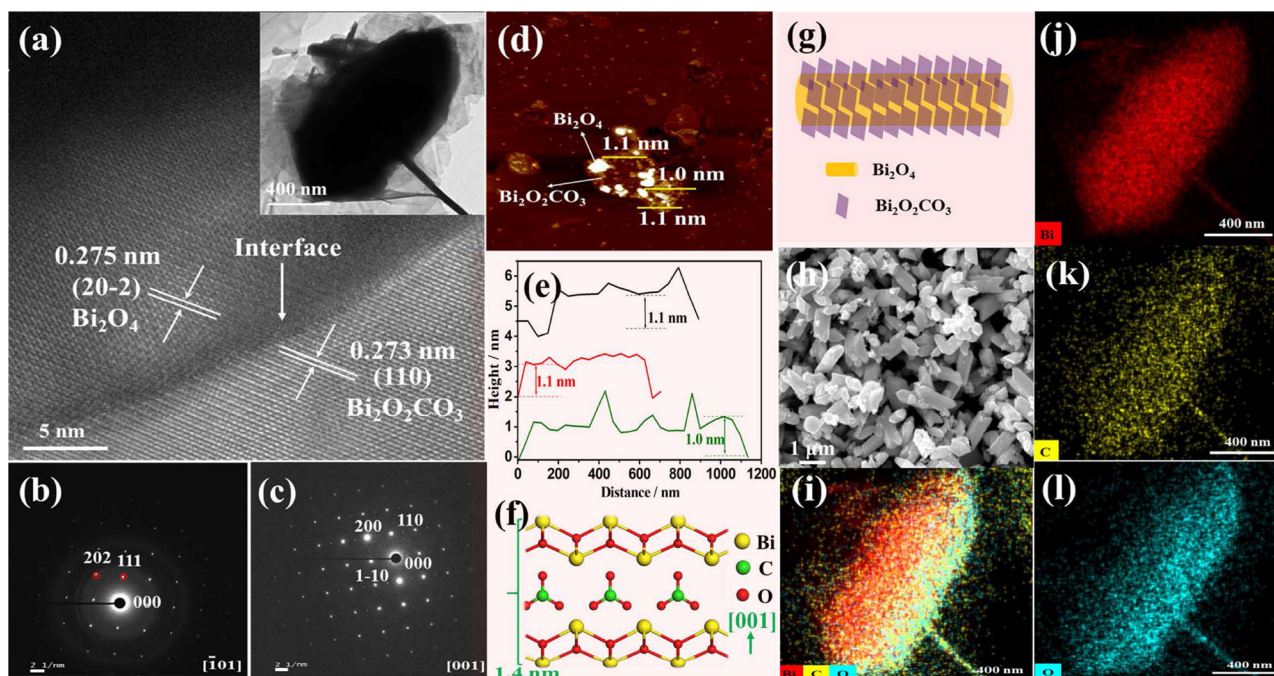
Fig. 1. (a) HRTEM image of $Bi_2O_4/Bi_2O_2CO_3$ composite (The inset was TEM images of $Bi_2O_4/Bi_2O_2CO_3$ composite obtained under LED lamp irradiation with the wavelength of 420 nm for 2 h). SAED images of (b) Bi_2O_4 and (c) $Bi_2O_2CO_3$. (d) AFM image of $Bi_2O_4/Bi_2O_2CO_3$ composite and (e) the corresponding height profiles. (f) Structure of one-unit-cell $Bi_2O_2CO_3$ layers grow within {001} facet. (g) Schematic diagram of $Bi_2O_4/Bi_2O_2CO_3$ heterojunction. (h) SEM image of pristine Bi_2O_4. (i–l) Elemental EDS-mapping images of $Bi_2O_4/Bi_2O_2CO_3$ heterostructure.
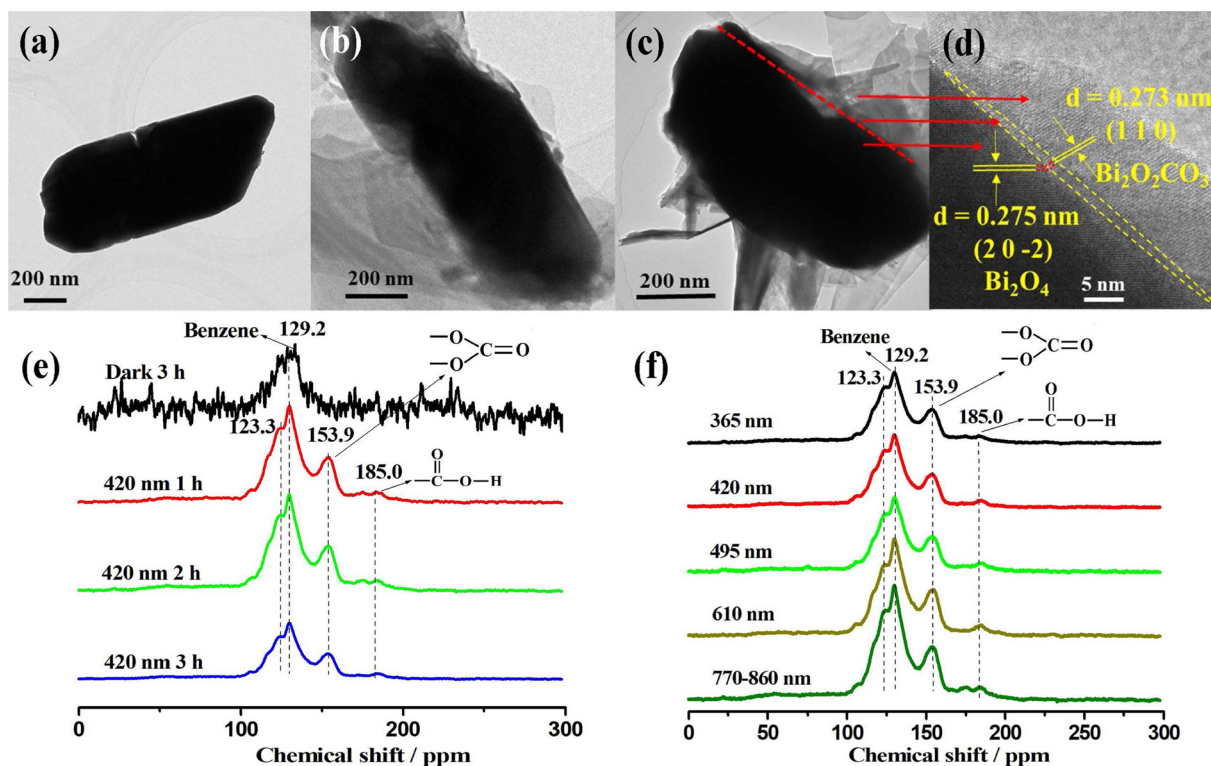

Fig. 2. The morphology of Bi_2O_4 obtained under LED lamp irradiation with the wavelength of 420 nm for (a) 0 h, (b) 1 h and (c) 2 h. (d) TEM image of $Bi_2O_4/Bi_2O_2CO_3$ heterostructures obtained under LED lamp irradiation with the wavelength of 420 nm for photocatalytic degradation of phenol for 2 h. Experimental ^{13}C NMR spectra of the Bi_2O_4 gained (e) under LED lamp irradiation with the wavelength of 420 nm for different time and (f) under LED lamps with different wavelength for 2 h for photocatalytic degradation of phenol.

percentage of undercoordinated Bi atoms. The fact with the highest surface energy will fade away rapidly in the crystal growth process for minimizing its total energy. While, the Bi_2O_4 with {-101} facets

exposed is obtained, which could be attributed to the synergetic effect of the weak alkali environment as the capping reagents reducing the surface energy [2]. The electronic structure of the Bi_2O_4 and $Bi_2O_4/$
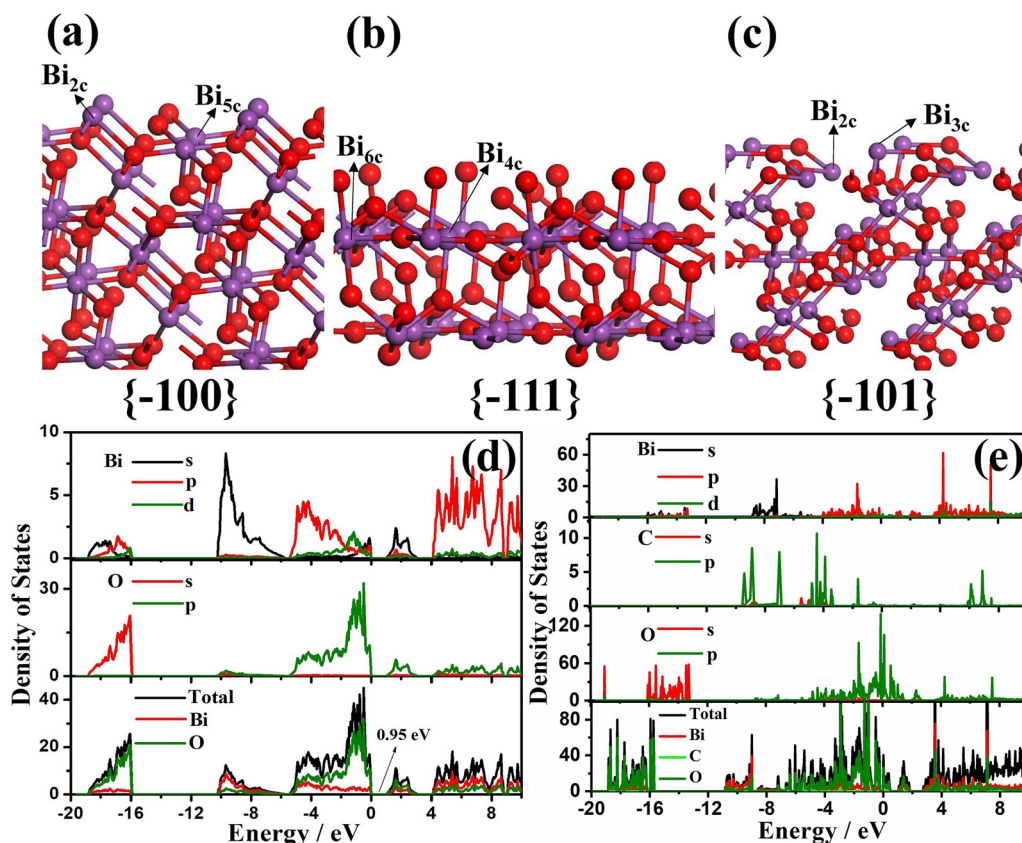
Fig. 3. The surface structures of the relaxed stoichiometric (a) {-100}, (b) {-111} and (c) {-101} facets. The calculations of total density of states (TDOS) and partial density of states (PDOS) of (d) Bi_2O_4 and (e) $Bi_2O_4/Bi_2O_2CO_3$.

$Bi_2O_2CO_3$ composite was further investigated. The bandgap of the {-101} facets of Bi_2O_4 was calculated to ~0.95 eV (Fig. 3d). The Bi_2O_4 coupled a certain amount of $Bi_2O_2CO_3$ with exposed {001} facets constituted a typical heterojunction photocatalyst system, and the valence band maximum (VBM) of the Bi_2O_4 shifts up, resulting from the hybridization of the Bi 4p and the O 2p orbits (Fig.3e). More interesting, the Bi_2O_4 displays increased charge density near the Fermi level after coupling $Bi_2O_2CO_3$. In that case, it can be anticipated that the $Bi_2O_4/Bi_2O_2CO_3$ composite will show enhanced photoresponsivity [43,44], which could be demonstrated by the following photoelectrochemical analysis.

The composition and valence state of elements of Bi_2O_4 nanocrystals and $Bi_2O_4/Bi_2O_2CO_3$ composite were further detected by XPS, which further demonstrates the presence of $Bi_2O_2CO_3$. As shown in Fig. 4a, it could be seen that Bi_2O_4 and $Bi_2O_4/Bi_2O_2CO_3$ are mainly composed by Bi, C and O elements. For Bi_2O_4, carbon element was originated from the XPS analysis instrument. Fig. 4b shows the Bi 4f spectrum and the corresponding fitting peaks of Bi_2O_4 and $Bi_2O_4/Bi_2O_2CO_3$ composite. The peaks of binding energies at 158.5, 159 and 163.7, 164.3 eV could be indexed to Bi $4f_{7/2}$ and Bi $4f_{5/2}$, respectively. The binding energies at 158.5 and 163.7 eV could be attributed to Bi^{3+}. Moreover, the binding energies at 159 and 164.3 eV are attributed to Bi^{5+} of the samples [45–48]. Comparing to pure Bi_2O_4, a positive shift is observed in the $Bi_2O_4/Bi_2O_2CO_3$ composite, indirectly demonstrating the heterojunction structure of $Bi_2O_4/Bi_2O_2CO_3$ composite and indicating the strong interaction between Bi_2O_4 and $Bi_2O_2CO_3$ [49]. Fig. 4c reveals the C 1 s spectrum of Bi_2O_4 and $Bi_2O_4/Bi_2O_2CO_3$ composite. The ranging of binding energy of samples from 280 to 290 eV could be divided to the binding energies of 284.6 and 288.3 eV for $Bi_2O_4/Bi_2O_2CO_3$ composite, 284.6 eV for Bi_2O_4. Whereas, the peak at 284.6 eV could be assigned to the extraneous carbon, and the peak at 288.3 eV could be ascribed to the carbon of one-unit-cell $Bi_2O_2CO_3$ layers [50,51]. The peaks for O 1s

could be fitted to 529.3, 530.2 and 531.2 for $Bi_2O_4/Bi_2O_2CO_3$ composite, and 529.2 and 531.3 eV for Bi_2O_4 (Fig. 4d). The peak at 529.3 or 529.2 eV could be attributed to the Bi-O bonds, and the peak at 531.2 or 531.3 eV might be attributed to the adsorbed H_2O on the surface of the materials [52,53]. While the peak at 530.2 eV for $Bi_2O_4/Bi_2O_2CO_3$ composite could be attributed to the carbonate species of $Bi_2O_4/Bi_2O_2CO_3$ composite [10,54]. The binding energy of Bi 4f and O 1s shows a positive shift, exhibiting that the interaction between Bi atoms and carbonate species resulted in the coating of the $Bi_2O_2CO_3$, which is not the physical adsorption.

UV-Vis-NIR diffuse reflection spectra (DRS) is a crucial criterion for evaluating the light absorption property of photocatalysts [55,56]. With increasing irradiation time, the optical absorption of the samples has the blue shift (Fig. 5a). The energy band gap (E_g) of the Bi_2O_4 can be estimated by using the expression $\alpha h\nu = A (h\nu - E_g)^n$, where ν and $h\nu$ are the absorption coefficient and the photon energy, respectively, and n is equal to 2 for Bi_2O_4 because of its indirect transition semiconductor property [57,58]. The band gap energy of Bi_2O_4 could be evaluated to be about ~1.63 eV (Fig. 5b). The introducing of $Bi_2O_2CO_3$ caused the blue shift of absorption spectra of Bi_2O_4, derived from the UV absorption property of $Bi_2O_2CO_3$. Fig. 5c shows the XPS valence band spectra of Bi_2O_4 and $Bi_2O_2CO_3$. The VB positions of Bi_2O_4 and $Bi_2O_2CO_3$ are determined to be located at ~1.55 eV and ~3.48 eV approximately by linear extrapolation, respectively. So the E_{CB} of Bi_2O_4 and $Bi_2O_2CO_3$ are equal to −0.08 and 0.22 eV, respectively (The band gap calculation of $Bi_2O_2CO_3$ can be seen in Fig. S7). The Bi_2O_4 nanocrystals possess a well full spectrum light responsible capacity for degradation of phenol, but one-unit-cell $Bi_2O_2CO_3$ layers is a wide-bandgap semiconductor, which is very difficult to be activated by visible light [59]. For this reason, it is vital and indispensable to explore the transfer and separation process of carriers. Therefore, the ns-level time-resolved fluorescence decay spectra of Bi_2O_4 nanocrystals and $Bi_2O_4/Bi_2O_2CO_3$ heterojunction were

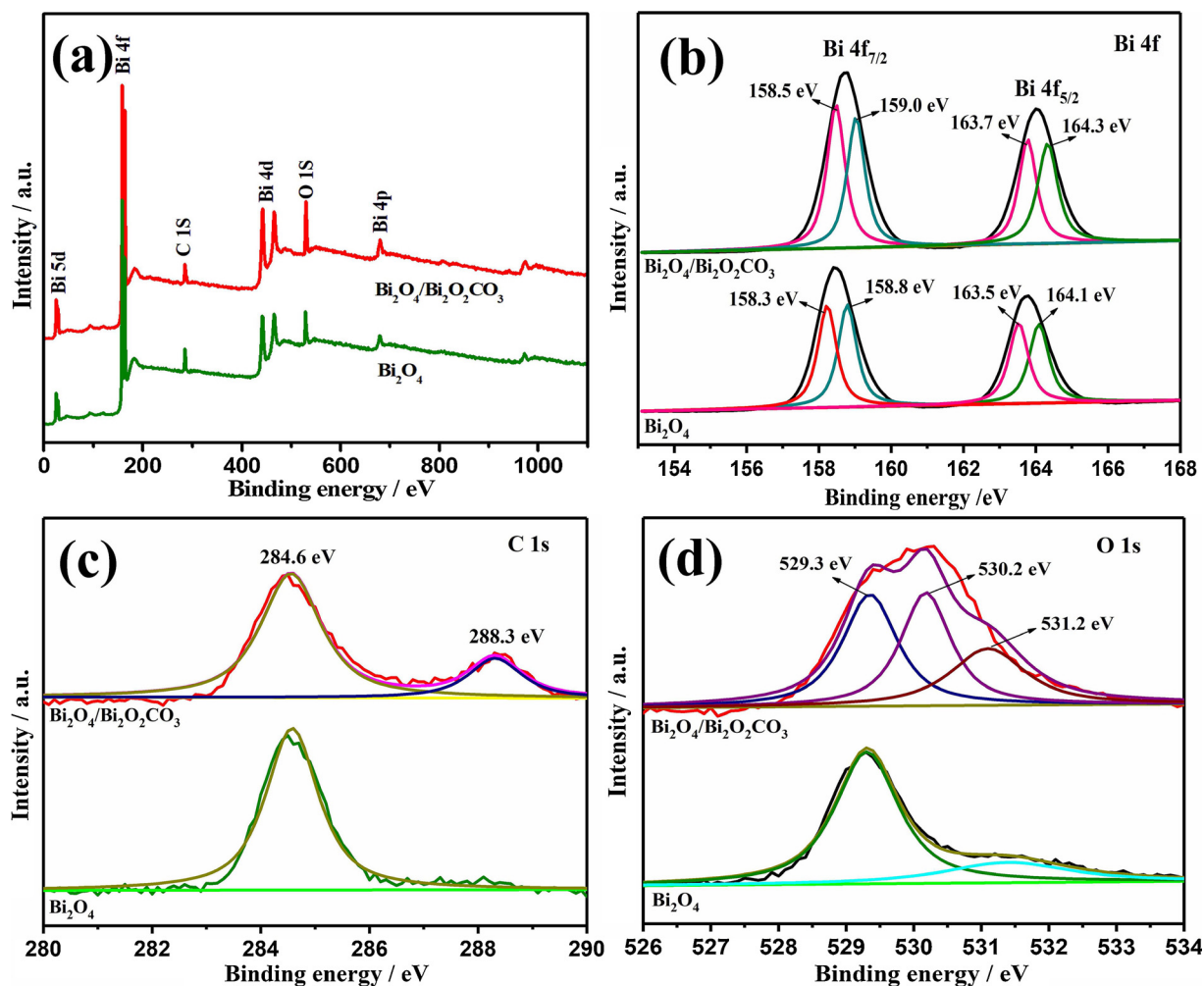**Fig. 4.** XPS spectra of Bi_2O_4 and $Bi_2O_4/Bi_2O_2CO_3$ composite: (a) wide survey spectra. (b–d) High-resolution spectra of Bi 4f, C 1s and O 1s, respectively.

studied (Fig. 5d). Table 1 reveals that the $< \tau >$ value of Bi_2O_4 nanosheets was decreased from 1.346 ns to 1.285 ns after introducing the one-until-cell $Bi_2O_2CO_3$ layers, indicating the emergence of a non-radiative pathway from the electronic interaction between Bi_2O_4 nanocrystals and one-until-cell $Bi_2O_2CO_3$ layers.

To better research the characteristics of charge separation at the interface between Bi_2O_4 and $Bi_2O_2CO_3$ and enhanced photocatalytic activity of $Bi_2O_4/Bi_2O_2CO_3$ composite, their surface work functions and electrochemical properties were observed. The work function of Bi_2O_4 (20-2) was approximately 4.295 eV, which was evidently lower than 4.410 eV for $Bi_2O_2CO_3$ (110) (Fig. S8). Once the $Bi_2O_2CO_3$ (110) coupled to Bi_2O_4, the electrons of Bi_2O_4 (20-2) will diffuse to $Bi_2O_2CO_3$ (110) until they share the same Fermi level. In the photocatalytic process, the electrons will transfer to the CB of $Bi_2O_2CO_3$, which can greatly inhibit the carrier recombination of $Bi_2O_4/Bi_2O_2CO_3$ composite (Fig. 6a). Fig. 6b describes the current-time (I-t) curves of Bi_2O_4 and $Bi_2O_4/Bi_2O_2CO_3$ composite under visible-light irradiation, which were used further to research the separation and transfer efficiency of photogenerated carriers in photocatalysis [60,61]. The photocurrent density of the $Bi_2O_4/Bi_2O_2CO_3$ photocatalyst is about 2 times larger than that of Bi_2O_4, indicating $Bi_2O_4/Bi_2O_2CO_3$ composite possessed the improved photoresponsivity, which is in accordance with the DFT calculated results, and higher light conversion efficiency and lower recombination rate of photogenerated carriers of $Bi_2O_4/Bi_2O_2CO_3$ nanocomposite, which is further demonstrated by their EIS Nyquist plots (Fig. 6c). It can be forecasted that the $Bi_2O_4/Bi_2O_2CO_3$ composite could exhibit superior photocatalysis for pollutants removal.

To evaluate the photocatalytic performances of the as-prepared samples under visible light irradiation, ciprofloxacin (CIP) and phenol were selected as the target pollutants. The photolysis result in Fig.7a shows that the only 6% CIP in aqueous solution could be degraded in the absence of photocatalyst, indicating that CIP in aqueous solution is stable. The dark adsorption experiment shows that about 18% CIP in aqueous solution could be adsorbed by $Bi_2O_4/Bi_2O_2CO_3$ composite. The photolysis and dark adsorption experiments confirm that the degradation of CIP in aqueous solution could be attributed to the photocatalysis. It can be obviously found that $Bi_2O_4/Bi_2O_2CO_3$ composite obtained under visible light irradiation for 2 h exhibited superior photocatalytic performance for degradation of CIP in aqueous solution compared to pure Bi_2O_4, $Bi_2O_2CO_3$ and $Bi_2O_4/Bi_2O_2CO_3$ composite obtained under visible light irradiation for 1 and 3 h. The degradation reaction of CIP can be simplified by a pseudo-first-order kinetics as follows:

$$\ln(C_0/C_t) = kt,$$

where C_t represents the concentration of CIP in aqueous solution after light irradiation, and C_0 is the initial concentration of CIP in aqueous solution. Fig. 7b shows the reaction kinetic curves of the as-prepared samples. The rate constants (k) are $4.8 \times 10^{-4}\,min^{-1}$, $1.00 \times 10^{-2}\,min^{-1}$, $8.71 \times 10^{-3}\,min^{-1}$, $1.25 \times 10^{-2}\,min^{-1}$ and $5.58 \times 10^{-3}\,min^{-1}$ for $Bi_2O_2CO_3$, Bi_2O_4, $Bi_2O_4/Bi_2O_2CO_3$ (1 h), $Bi_2O_4/Bi_2O_2CO_3$ (2 h) and $Bi_2O_4/Bi_2O_2CO_3$ (3 h), respectively. It can be found that the photocatalytic reaction rate over $Bi_2O_4/Bi_2O_2CO_3$ (2 h) is 1.25 times higher than that of pure Bi_2O_4. In addition, the photocatalytic performance of

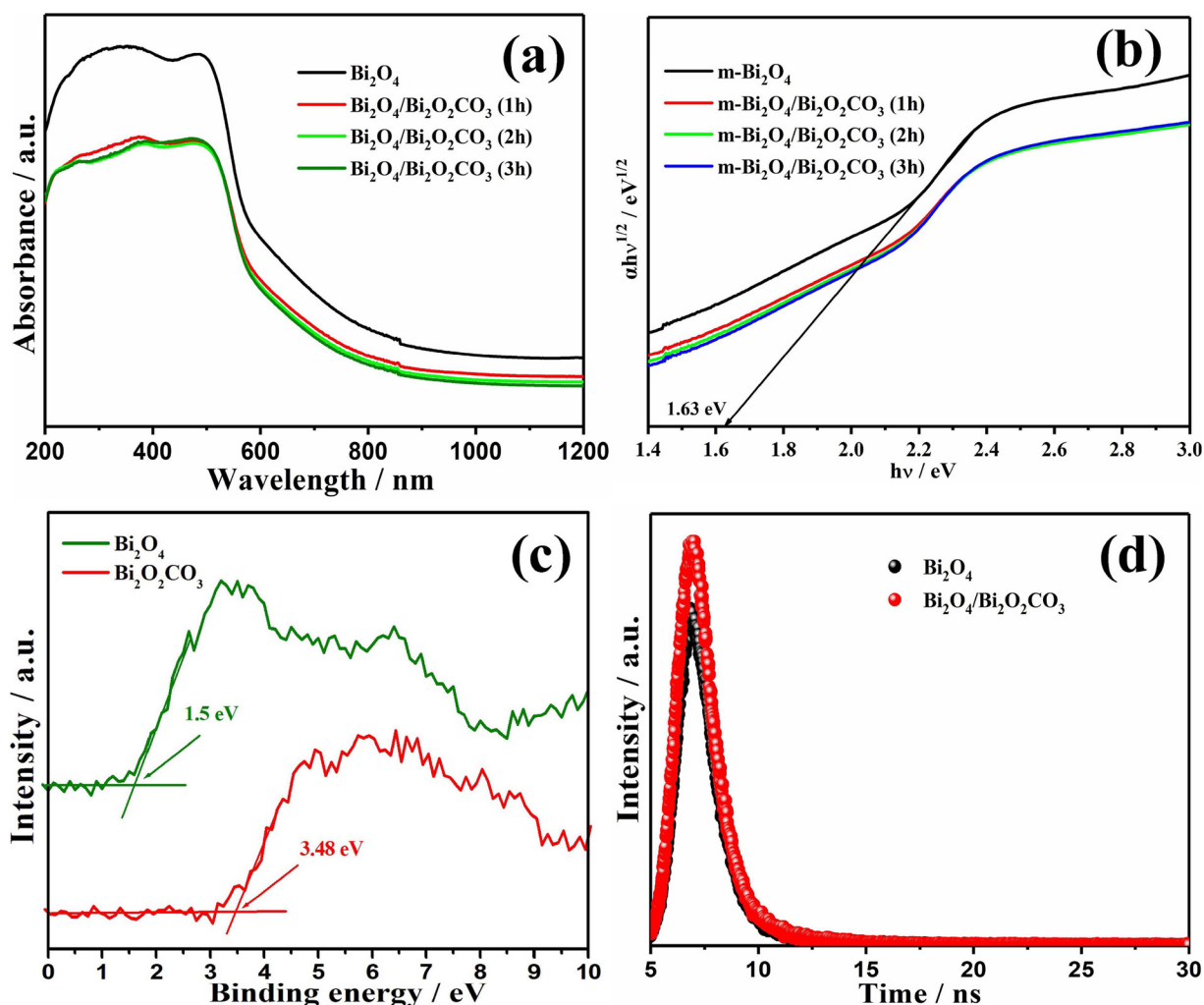**Fig. 5.** (a) The optical absorption spectra and (b) plot of $\alpha h\upsilon$ versus energy ($h\upsilon$) for the band gap energy of Bi_2O_4, $Bi_2O_4/Bi_2O_2CO_3$ composite formed after 1–3 h of exposure under visible light irradiation. (c) XPS valance band spectra of Bi_2O_4, $Bi_2O_4/Bi_2O_2CO_3$ which was irradiated for 2 h in RhB aqueous solution. (d) Nanosecond-level time-resolved fluorescence spectra at room temperature for Bi_2O_4 and $Bi_2O_4/Bi_2O_2CO_3$.

Table 1
Kinetic parameters of the fitting decay parameters of Bi_2O_4 and $Bi_2O_4/Bi_2O_2CO_3$.

Samples	parameters	lifetime/ns	χ^2
Bi_2O_4	τ_1	0.562	1.102
	τ_2	0.641	
	τ_3	2.587	
	$<\tau>$	1.346	
$Bi_2O_4/Bi_2O_2CO_3$	τ_1	0.524	1.168
	τ_2	0.656	
	τ_3	2.297	
	$<\tau>$	1.285	

the as-prepared samples was further assessed by degrading phenol under visible light irradiation (Fig. 7c). The $Bi_2O_4/Bi_2O_2CO_3$ nanocomposite exhibited 99% photocatalytic efficiency for phenol degradation, which is better than the mechanical mixed $Bi_2O_4/Bi_2O_2CO_3$. Moreover, the kinetic constant of phenol degradation by $Bi_2O_4/Bi_2O_2CO_3$ nanocomposite is nearly 1.73 times higher than that by Bi_2O_4 nanocrystals (Fig. 7d). As we know, the total organic carbon (TOC) is a crucial index to measure the mineralization rate of the organic pollutants. As shown in Fig. 7e, the degradation rate of the phenol is positive correlation to its mineralization rate. The $Bi_2O_4/Bi_2O_2CO_3$ composite showed more efficient mineralization as compared to pure Bi_2O_4.

Beyond that, $Bi_2O_4/Bi_2O_2CO_3$ could still possess photocatalytic degradation ratio of 94% for phenol after five circles under visible light irradiation (Fig. 7f). Besides, the trapping experiments have also been carried out to investigation the active species in photocatalytic process. Isopropyl alcohol (IPA) and sodium oxalate ($Na_2C_2O_4$) are chosen to be as the scavengers of •OH and h^+, respectively, and nitroblue tetrazolium (NBT) is used to detect the generation of $\cdot O_2^-$ [62–69]. Fig. S9a shows that the degradation performance of phenol in aqueous solution decreases obviously after adding $Na_2C_2O_4$, while the degradation activity has a little decrease after adding IPA. Moreover, the absorbance change of NBT in aqueous solution in the presence of $Bi_2O_4/Bi_2O_2CO_3$ composite under visible light irradiation is negligible (Fig. S9b). The results demonstrate h^+ plays the dominant part in the photocatalytic degradation of phenol in aqueous solution, while $\cdot OH$ and $\cdot O_2^-$ plays the minor role.

In addition, the intermediate products of CIP in aqueous solution during photocatalytic degradation process were investigated by liquid chromatograph-mass spectrometer (LC–MS). According the analysis of mass spectrometry, the main transformation products can be identified and products with m/z of 366.0, 310.0, 298.0, 296.0, 282.0, 280.0 and 274.0 could be attributed to the degraded products of CIP in aqueous solution (Fig. S10). The chemical structure of the corresponding products was summarized in Table S1 based on the mass spectra and reported works [70–72]. The concentrations of the products with m/z of 298.0, 296.0, 282.0, 280.0 and 274 are very high, confirming these five
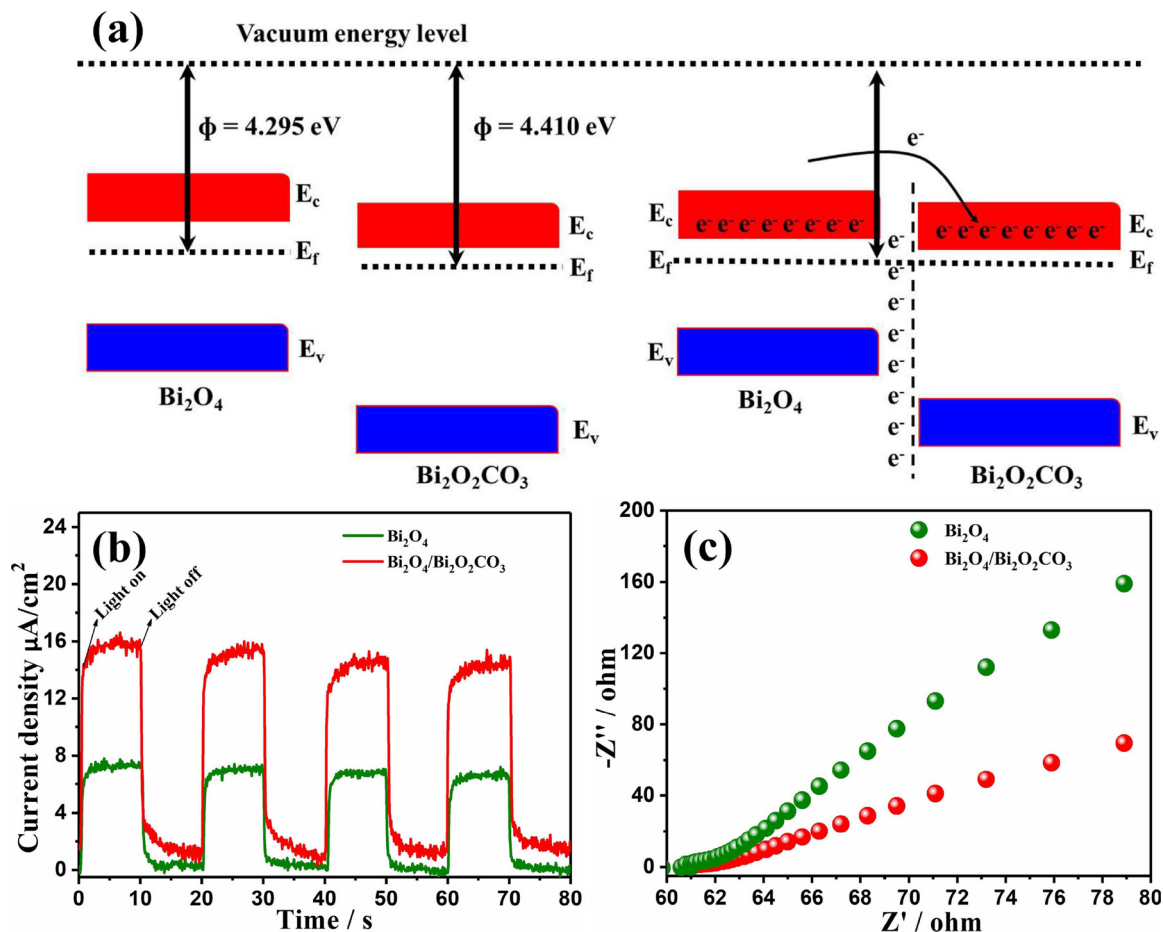
Fig. 6. (a) The work functions of Bi_2O_4 with (20-2) surface and $Bi_2O_2CO_3$ with (110) surface. (b) The photocurrent responses and (c) the EIS-Nyquist plots of pure Bi_2O_4, the $Bi_2O_4/Bi_2O_2CO_3$ photocatalyst electrodes in 0.1 M Na_2SO_4 aqueous solution under visible light irradiation.
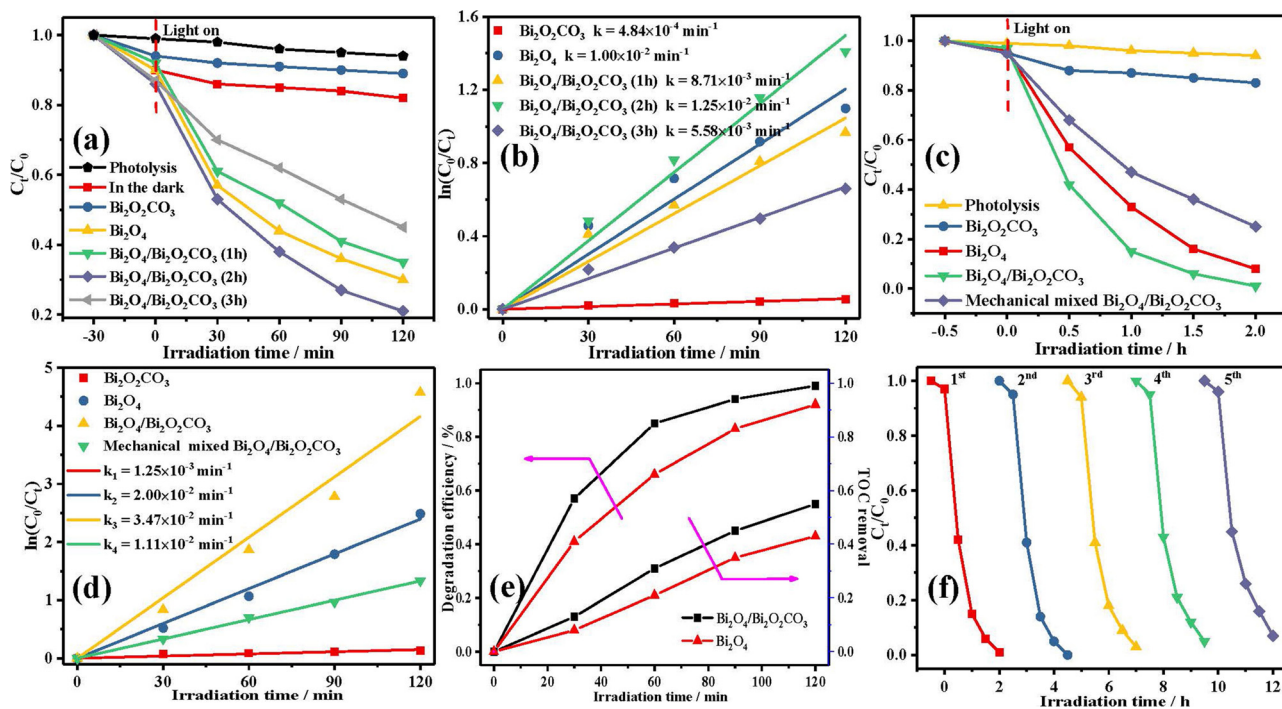
Fig. 7. (a, c) Photocatalytic activities of the as-prepared photocatalysts for the degradation of CIP and phenol in aqueous solution, respectively, and (b, d) the corresponding kinetic analysis. (e) Degradation and TOC removal of phenol under the photocatalytic process in the presence of the photocatalysts. (f) Photocatalytic degradation of phenol over $Bi_2O_4/Bi_2O_2CO_3$ composite during cycling operation with exposure to visible light.
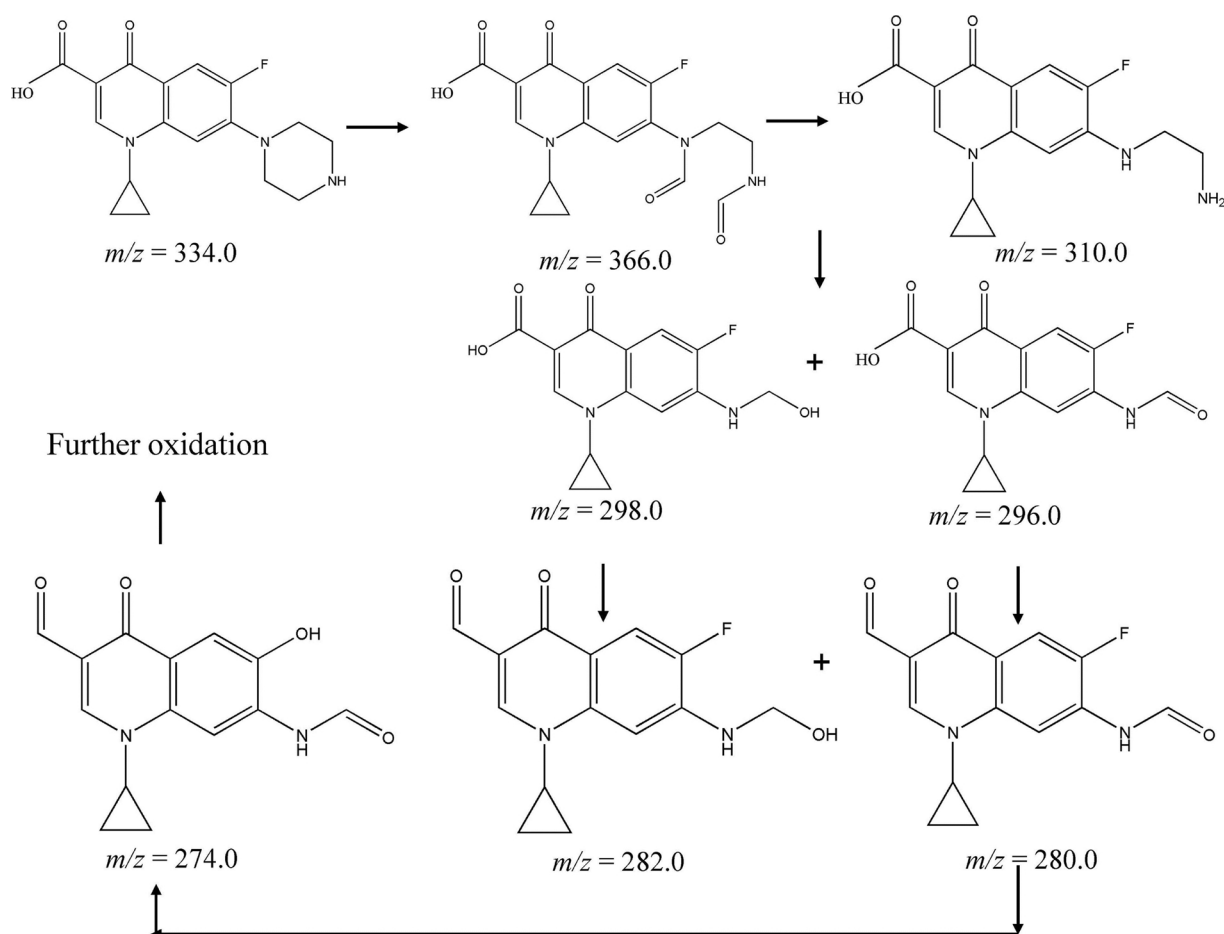
Fig. 8. Proposed degradation pathways of ciprofloxacin in aqueous solution by $Bi_2O_4/Bi_2O_2CO_3$ composite under visible light irradiation.

by-products may be produced in the photocatalytic degradation of CIP in aqueous solution. The results show that CIP in aqueous solution is photocatalytic degraded by breaking the piperazine ring rather than the quinolone moiety breakage. According to the results, the possible reaction pathways can be proposed in Fig. 8.

Based on the above analyses, a possible formation mechanism of $Bi_2O_4/Bi_2O_2CO_3$ heterojunction can be depicted as Fig. 9a. In the first stage, the organic pollutants were adsorbed on the surface of Bi_2O_4 nanocrystals, and the pollutants were gradually degraded by Bi_2O_4 photocatalyst into intermediate products, CO_2 and H_2O under UV, visible and NIR lights irradiation. In the second stage, prior to decompose into CO_2 and H_2O, the intermediate products were adsorbed and further recombined with the undercoordinated Bi atoms on the {-101} facets of Bi_2O_4. In the third stage, the $Bi_2O_2CO_3$ sheets were generated and in-situ epitaxial growth on the surface of Bi_2O_4 nanocrystals. Finally, the $Bi_2O_4/Bi_2O_2CO_3$ heterostructure has been successfully obtained. In the $Bi_2O_4/Bi_2O_2CO_3$ heterostructure, the photogenerated electrons transfer path can be illustrated as Fig. 9b, in the first, the Bi_2O_4 photocatalyst is activated under the UV, visible or NIR light irradiation, the photoexcited electrons could quickly transfer from the excited Bi_2O_4 to the CB of $Bi_2O_2CO_3$, because the CB position of Bi_2O_4 is more negative than that of $Bi_2O_2CO_3$. The electrons on the CB of $Bi_2O_2CO_3$ would react with resolved O_2 and H^+ to generate H_2O_2, which could be further reduced to ·OH radicals [47]. Finally, the left photoexcited h^+ in the VB of Bi_2O_4 and ·OH would attack pollutant molecular causing the mineralization of pollutants. Remarkably, $Bi_2O_2CO_3$ facilitates the separation of the photogenerated electrons from the CB of Bi_2O_4, resulting in the higher photocatalytic rate for CIP and phenol removal.

4. Conclusions

The $Bi_2O_4/Bi_2O_2CO_3$ heterojunction was successfully synthesized by light induced in-situ epitaxy of one-unit-cell $Bi_2O_2CO_3$ layers on Bi_2O_4 nanocrystals. The well-matched lattice parameters between the $Bi_2O_2CO_3$ and Bi_2O_4 are crucial for the assembling of epitaxial heterostructures. The solid-state ^{13}C NMR spectra demonstrated carbon source in $Bi_2O_4/Bi_2O_2CO_3$ structure was derived from the phenol, which could be transformed in the photocatalytic process. Profiting from exposed {-101} facets with larger percentage of undercoordinated Bi atoms, the one-unit-cell $Bi_2O_2CO_3$ layers could successfully grow on the Bi_2O_4 nanocrystals by an epitaxial mean. Benefit from the epitaxial growth of one-unit-cell $Bi_2O_2CO_3$ layers, the $Bi_2O_4/Bi_2O_2CO_3$ heterostructure reveals enhanced photocatalytic activity for degradation of phenol and CIP in aqueous solution. The possible intermediates and degradation pathways of CIP in aqueous solution were also analyzed. The present work provides a new thought for constructing highly efficient Bi-based epitaxial heterostructures.

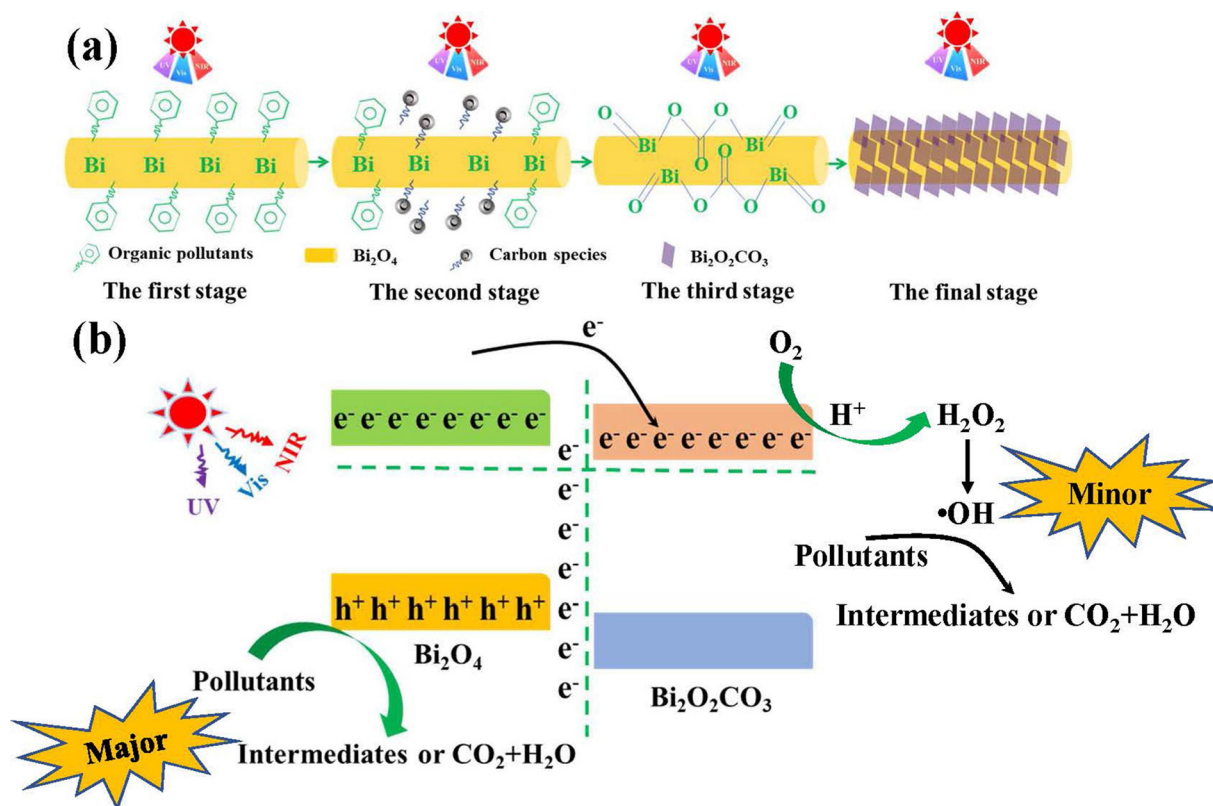**Fig. 9.** (a) Schematic illustration of the formation process of $Bi_2O_4/Bi_2O_2CO_3$ heterostructure. (b) Proposed photo-generated electrons transfer path of $Bi_2O_4/Bi_2O_2CO_3$ composite at its interface.

Appendix A. Supplementary data

Supplementary data associated with this article can be found, in the online version, at https://doi.org/10.1016/j.apcatb.2018.10.067.

References

[1] M. Navlani-García, P. Verma, Y. Kuwahara, T. Kamegawa, K. Mori, H. Yamashita, Visible-light-enhanced catalytic activity of Ru nanoparticles over carbon modified g-C$_3$N$_4$, J. Photochem. Photobiol. A 258 (2018) 327–333.

[2] Y. Zhang, W.Q. Cui, W.J. An, L. Liu, Y.H. Liang, Y.F. Zhu, Combination of photo-electrocatalysis and adsorption for removal of bisphenol A over TiO$_2$-graphene hydrogel with 3D network structure, Appl. Catal. B: Environ. 221 (2018) 36–46.

[3] X. Hai, K. Chang, H. Pang, M. Li, P. Li, H.M. Liu, L. Shi, J.H. Ye, Engineering the edges of MoS$_2$ (WS$_2$) crystals for direct exfoliation into monolayers in polar micromolecular solvents, J. Am. Chem. Soc. 138 (2016) 14962–14969.

[4] D.Q. Zhang, M.C. Wen, S.S. Zhang, P.J. Liu, W. Zhu, G.S. Li, H.X. Li, Au nanoparticles enhanced rutile TiO$_2$ nanorod bundles with high visible-light photocatalytic performance for NO oxidation, Appl. Catal. B: Environ. 147 (2018) 610–616.

[5] H. Li, F. Qin, Z.P. Yang, X.M. Cui, J.F. Wang, L.Z. Zhang, New reaction pathway induced by plasmon for selective benzyl alcohol oxidation on BiOCl possessing oxygen vacancies, J. Am. Chem. Soc. 139 (2017) 3513–3521.

[6] P. Verma, Y. Kuwahara, K. Mori, H. Yamashita, Synthesis of mesoporous silica-supported Ag nanorod-based bimetallic catalysts and investigation of their plasmonic activity under visible light irradiation, Catal. Sci. Technol. 7 (2017) 2551–2558.

[7] X. Wang, Y.H. Liang, W.J. An, J.S. Hu, Y.F. Zhu, W.Q. Cui, Removal of chromium (VI) by a self-regenerating and metal free g-C$_3$N$_4$/graphene hydrogel system via the synergy of adsorption and photo-catalysis under visible light, Appl. Catal. B: Environ. 219 (2017) 53–62.

[8] C.F. Mu, Y. Zhang, W.Q. Cui, Y.H. Liang, Y.F. Zhu, Removal of bisphenol A over a separation free 3D Ag$_3$PO$_4$-graphene hydrogel via an adsorption-photocatalysis synergy, Appl. Catal. B: Environ. 212 (2017) 41–49.

[9] J. Li, J. Wang, G.K. Zhang, Y. Li, K. Wang, Enhanced molecular oxygen activation of Ni^{2+}-doped BiO$_{2-x}$ nanosheets under UV, visible and near-infrared irradiation: mechanism and DFT study, Appl. Catal. B: Environ. 234 (2018) 167–177.

[10] P. Madhusudan, J. Zhang, B. Cheng, G. Liu, Photocatalytic degradation of organic dyes with hierarchical Bi$_2$O$_2$CO$_3$ microstructures under visible-light, CrystEngComm 15 (2013) 231–240.

[11] R. Zhang, Y. Dai, Z.Z. Lou, Z.J. Li, Z.Y. Wang, Y.M. Yang, X.Y. Qin, X.Y. Zhang, B.B. Huang, Layered photocatalyst Bi$_2$O$_2$[BO$_2$(OH)] nanosheets with internal polar field enhanced photocatalytic activity, CrystEngComm 16 (2014) 4931–4934.

[12] X.Y. Wu, M.M. Li, J. Li, G.K. Zhang, S. Yin, A sillenite-type Bi$_{12}$MnO$_{20}$ photocatalyst: UV, visible and infrared lights responsive photocatalytic properties induced by the hybridization of Mn 3d and O 2p orbitals, Appl. Catal. B: Environ. 219 (2017) 132–141.

[13] T.G. Zhou, Y.F. Zhang, M.S. Lin, J.L. Long, Z.Z. Zhang, H.X. Lin, J.C.S. Wu, X.X. Wang, Monolayered Bi$_2$WO$_6$ nanosheets mimicking heterojunction interface with open surfaces for photocatalysis, Nat. Commun. 6 (2015) 8340.

[14] H.F. Cheng, B.B. Huang, Y. Dai, Engineering BiOX (X = Cl, Br, I) nanostructures for highly efficient photocatalytic applications, Nanoscale 6 (2014) 2009–2026.

[15] H.G. Yu, C. Cao, X.F. Wang, J.G. Yu, Ag-modified BiOCl single-crystal nanosheets: dependence of photocatalytic performance on the region-selective deposition of Ag nanoparticles, J. Phys. Chem. C 121 (2017) 13191–13201.

[16] Y.C. Hong, K.Q. Sun, K.H. Han, G. Liu, B.Q. Xu, Comparison of catalytic combustion of carbon monoxide and formaldehyde over Au/ZrO$_2$ catalysts, Catal. Today 158 (2010) 415–422.

[17] H.G. Yu, W.J. Liu, X.F. Wang, F.Z. Wang, Promoting the interfacial H$_2$-evolution reaction of metallic Ag by Ag$_2$S cocatalyst: a case study of TiO$_2$/Ag-Ag$_2$S photocatalyst, Appl. Catal. B: Environ. 225 (2018) 415–423.

[18] C.X. Pan, J. Xu, Y.J. Wang, D. Li, Y.F. Zhu, Dramatic activity of C$_3$N$_4$/BiPO$_4$ photocatalyst with core/shell structure formed by self-assembly, Adv. Funct. Mater. 22 (2012) 1518–1524.

[19] S.S. Song, J.M. Wang, T.Y. Peng, W.L. Fu, L. Zan, MoS$_2$-MoO$_{3-x}$ hybrid cocatalyst for effectively enhanced H$_2$ production photoactivity of AgIn$_5$S$_8$ nano-octahedrons, Appl. Catal. B: Environ. 228 (2018) 39–46.

[20] Y.X. Deng, M.Y. Xing, J.L. Zhang, An advanced TiO$_2$/Fe$_2$TiO$_5$/Fe$_2$O$_3$ triple-heterojunction with enhanced and stable visible-light-driven fenton reaction for the removal of organic pollutants, Appl. Catal. B: Environ. 211 (2017) 157–166.

[21] T. Xiong, M.Q. Wen, F. Dong, J.Y. Yu, L.L. Han, B. Lei, Y.X. Zhang, X.S. Tang, Z.G. Zang, Three dimensional Z-scheme (BiO)$_2$CO$_3$/MoS$_2$ with enhanced visible light photocatalytic NO removal, Appl. Catal. B: Environ. 199 (2016) 87–95.

[22] X. Chen, D.F. Peng, Q. Ju, F. Wang, Photon upconversion in core-shell nanoparticles, Chem. Soc. Rev. 44 (2015) 1318–1330.

[23] H.L. Wen, H. Zhu, T.F. Hung, B.L. Wang, G.Y. Zhu, S.F. Yu, F. Wang, Upconverting near-infrared light through energy management in core-shell-shell nanoparticles, Angew. Chem. Int. Ed. 52 (2013) 13419–13423.

[24] C.L. Tan, H. Zhang, Epitaxial growth of hetero-nanostructures based on ultrathin two-dimensional nanosheets, J. Am. Chem. Soc. 137 (2015) 12162–12174.

[25] M.F. Shao, F.Y. Ning, D.G. Evans, X. Duan, Hierarchical nanowire arrays based on ZnO core-layered double hydroxide shell for largely enhanced photoelectrochemical water splitting, Adv. Funct. Mater. 24 (2014) 580–586.

[26] Y. Hou, T.Z. Huang, Z.H. Wen, S. Mao, S.M. Cui, J.H. Chen, Metal-organic

framework-derived nitrogen-doped core-shell-structured porous Fe/Fe$_3$C@C nanoboxes supported on graphene sheets for efficient oxygen reduction reactions, Adv. Energy Mater. 4 (2014) 1400337.

[27] Z.W. Zhang, P. Chen, X.D. Duan, K.T. Zang, J. Luo, X.F. Duan, Robust epitaxial growth of two-dimensional heterostructures, multiheterostructures, and superlattices, Science 357 (2017) 788–792.

[28] X.L. Zhou, Y. Liu, H.X. Ju, B.C. Pan, J.F. Zhu, T. Ding, C.D. Wang, Q. Yang, Design and epitaxial growth of MoSe$_2$-NiSe vertical heteronanostructures with electronic modulation for enhanced hydrogen evolution reaction, Chem. Mater. 28 (2016) 1838–1846.

[29] M. Nakano, Y. Wang, Y. Kashiwabara, H. Matsuoka, Y. Iwasa, Layer-by-layer epitaxial growth of scalable WSe$_2$ on sapphire by molecular beam epitaxy, Nano Lett. 17 (2017) 5595–5599.

[30] Z.J. Yang, T. Altantzis, D. Zanaga, S. Bals, G.V. Tendeloo, M.P. Pileni, Supracrystalline colloidal eggs: epitaxial growth and freestanding three-dimensional supracrystals in nanoscaled colloidosomes, J. Am. Chem. Soc. 138 (2016) 3493–3500.

[31] J.Z. Chen, X.J. Wu, Y. Gong, Y.H. Zhu, Z.Z. Yang, B. Li, Q.P. Lu, Y.F. Yu, S.K. Han, Z.C. Zhang, Y. Zong, Y. Han, L. Gu, H. Zhang, Edge epitaxy of two-dimensional MoSe$_2$ and MoS$_2$ nanosheets on one-dimensional nanowires, J. Am. Chem. Soc. 139 (2017) 8653–8660.

[32] L. Fu, F. Wang, B. Wu, N. Wu, W. Huang, H.L. Wang, C.H. Jin, L. Zhang, J. He, L. Fu, Y.Q. Liu, Van der Waals epitaxial growth of atomic layered HfS$_2$ crystals for ultrasensitive near-infrared phototransistors, Adv. Mater. 29 (2017) 1700439.

[33] J. Demuth, E. Fahrenkrug, L.Y. Ma, T. Shodiya, J.I. Deitz, T.J. Grassman, S. Maldonado, Electrochemical liquid phase epitaxy (ec-LPE): a new methodology for the synthesis of crystalline group IV semiconductor epifilms, J. Am. Chem. Soc. 139 (2017) 6960–6968.

[34] X.C. Huang, J.Q. Guan, Z.J. Lin, B. Liu, S.Y. Xing, W.H. Wang, J.D. Guo, Epitaxial growth and band structure of Te film on graphene, Nano Lett. 17 (2017) 4619–4623.

[35] G. Kresse, J. Furthmüller, Efficient iterative schemes for ab initio total-energy calculations using a plane-wave basis set, Phys. Rev. B 54 (1996) 11169–11186.

[36] J.P. Perdew, K. Burke, M. Ernzerhof, Generalized gradient approximation made simple, Phys. Rev. Lett. 77 (1996) 3865–3868.

[37] G. Kresse, D. Joubert, From ultrasoft pseudopotentials to the projector augmented-wave method, Phys. Rev. B 59 (1999) 1758–1775.

[38] D. Zhang, S. Wang, J. Zhu, H. Li, Y. Lu, WO$_3$ nanocrystals with tunable percentage of (001)-facet exposure, Appl. Catal. B: Environ. 123 (2012) 398–404.

[39] J.P. Liu, J. Jiang, C.W. Cheng, H.X. Li, J.X. Zhang, H. Gong, H.J. Fan, Energy storage: Co$_3$O$_4$ nanowire@MnO$_2$ultrathin nanosheet core/shell arrays: a new class of high-performance pseudocapacitive materials, Adv. Mater. 23 (2011) 2075.

[40] J.K. Moore, M.A. Sakwa-Novak, W. Chaikittisilp, A.K. Mehta, M.S. Conradi, C.W. Jones, S.E. Hayes, Characterization of a mixture of CO$_2$ adsorption products in hyperbranched aminosilica adsorbents by ^{13}C solid-state NMR, Environ. Sci. Technol. 49 (2015) 13684–13691.

[41] I. Sheikhshoaiea, S.Y. Ebrahimipour, M. Sheikhshoaie, H.A. Rudbari, M. Khaleghi, G. Bruno, Combined experimental and theoretical studies on the X-ray crystal structure, FT-IR, ^{1}H NMR, ^{13}C NMR, UV–vis spectra, NLO behavior and antimicrobial activity of 2-hydroxyacetophenone benzoylhydrazone, Spectrochim. Acta A 124 (2014) 548–555.

[42] S. Sundarapandiyan, T.S. Renitha, J. Sridevi, P. Saravanan, B. Chandrasekaran, G.B. Raju, Photocatalytic degradation of highly refractive phenolic polymer-mechanistic insights as revealed by electron spin resonance (ESR) and solid-state ^{13}C NMR spectroscopy, Chem. Eng. J. 313 (2017) 1112–1121.

[43] M. Madl, W. Brezna, P. Klang, A.M. Andrews, G. Strasser, J. Smoliner, High resolution photocurrent imaging by atomic force microscopy on the example of single buried InAs quantum dots, Semicond. Sci. Technol. 25 (2010) 065010.

[44] X.D. Zhang, X. Xie, H. Wang, J.J. Zhang, B.C. Pan, Y. Xie, Enhanced photoresponsive ultrathin graphitic-phase C$_3$N$_4$ nanosheets for bioimaging, J. Am. Chem. Soc. 135 (2013) 18–21.

[45] W.J. Wang, X.Q. Chen, G. Liu, Z.R. Shen, D.H. Xia, P.K. Wong, J.C. Yu, Monoclinic dibismuth tetraoxide: a new visible-light-driven photocatalyst for environmental remediation, Appl. Catal. B: Environ. 176 (2015) 444–453.

[46] D.H. Xia, W.J. Wang, R. Yin, Z.F. Jian, T.C. An, G.Y. Li, H.J. Zhao, P.K. Wong, Enhanced photocatalytic inactivation of Escherichia coli by a novel Z-scheme g-C$_3$N$_4$/m-Bi$_2$O$_4$hybrid photocatalyst under visible light: the role of reactive oxygen species, Appl. Catal. B: Environ. 214 (2017) 23–33.

[47] M. Sun, S.L. Li, T. Yan, P.G. Ji, X. Zhao, K. Yuan, D. Wei, B. Du, Fabrication of heterostructured Bi$_2$O$_2$CO$_3$/Bi$_2$O$_4$ photocatalyst and efficient photodegradation of organic contaminants under visible-light, J. Hazard. Mater. 333 (2017) 169–178.

[48] J.X. Wang, K. Chen, Y. Shen, X. Wang, Y.F. Guo, X.J. Zhou, R.B. Bai, Enhanced photocatalytic degradation for organic pollutants by a novel m-Bi$_2$O$_4$/Bi$_2$O$_2$CO$_3$ photocatalyst under visible light, Res. Chem. Intermed. 44 (2018) 3061–3079.

[49] J. Zhu, S.H. Wang, J.G. Wang, D.Q. Zhang, H.X. Li, Highly active and durable Bi$_2$O$_3$/TiO$_2$ visible photocatalyst in flower-like spheres with surface-enriched Bi$_2$O$_3$ quantum dots, Appl. Catal. B: Environ. 102 (2011) 120–125.

[50] H.W. Huang, X.W. Li, J.J. Wang, F. Dong, P.K. Chu, T.R. Zhang, Y.H. Zhang, Anionic group self-doping as a promising strategy: band-gap engineering and multi-

[51] functional applications of high-performance CO$_3$$^{2-}$-doped Bi$_2O_2CO_3$, ACS Catal. 5 (2015) 4094–4103.

[51] Y. Huang, D.D. Zhu, Q. Zhang, Y.F. Zhang, J.J. Cao, Z.X. Shen, W.K. Ho, S.C. Lee, Synthesis of a Bi$_2$O$_2$CO$_3$/ZnFe$_2$O$_4$ heterojunction with enhanced photocatalytic activity for visible light irradiation-induced NO removal, Appl. Catal. B: Environ. 234 (2011) 70–78.

[52] K. Wang, G.K. Zhang, J. Li, Y. Li, X.Y. Wu, 0D/2D Z-scheme heterojunctions of bismuth tantalate quantum dots/ultrathin g-C$_3$N$_4$ nanosheets for highly efficient visible light photocatalytic degradation of antibiotics, ACS Appl. Mater. Interfaces 9 (2017) 43704–43715.

[53] Z. Wan, G.K. Zhang, Synthesis and facet-dependent enhanced photocatalytic activity of Bi$_2$SiO$_5$/AgI nanoplate photocatalysts, J. Mater. Chem. A 3 (2015) 16737–16745.

[54] P. Madhusudan, J.G. Yu, W.G. Wang, B. Cheng, G. Liu, Facile synthesis of novel hierarchical graphene-Bi$_2$O$_2$CO$_3$ composites with enhanced photocatalytic performance under visible light, Dalton Trans. 41 (2012) 14345–14353.

[55] J. Tian, Y.H. Sang, G.W. Yu, H.D. Jiang, X.N. Mu, H. Liu, A Bi$_2$WO$_6$-based hybrid photocatalyst with broad spectrum photocatalytic properties under UV, visible, and near-infrared irradiation, Adv. Mater. 25 (2013) 5075–5080.

[56] D.D. Tang, J. Li, G.K. Zhang, A novel open–framework spheniscidite photocatalyst with excellent visible light photocatalytic activity: silver sensitization effect and DFT study, Appl. Catal. B: Environ. 224 (2018) 433–441.

[57] X.Y. Wu, J.T. Wang, G.K. Zhang, K. Katsumata, K. Yanag-isawa, T. Sato, S. Yin, Series of M$_x$WO$_3$/ZnO (M = K, Rb, NH$_4$) nanocomposites: combination of energy saving and environmental decontamination functions, Appl. Catal. B: Environ. 201 (2017) 128–136.

[58] M.L. Guan, C. Xiao, J. Zhang, S.J. Fan, R. An, Q.M. Cheng, J.F. Xie, M. Zhou, B.J. Ye, Y. Xie, Vacancy associates promoting solar-driven photocatalytic activity of ultrathin bismuth oxychloride nanosheets, J. Am. Chem. Soc. 135 (2013) 10411–10417.

[59] Y.Y. Liu, Z.Y. Wang, B.B. Huang, K.S. Yang, X.Y. Zhang, X.Y. Qin, Y. Dai, Preparation, electronic structure, and photocatalytic properties of Bi$_2$O$_2$CO$_3$ nanosheet, Appl. Surf. Sci. 257 (2010) 172–175.

[60] L. Zhao, X.F. Chen, X.C. Wang, Y.J. Zhang, W. Wei, Y.H. Sun, M. Antonietti, M.M. Titirici, One-step solvothermal synthesis of a carbon@TiO$_2$ dyade structure effectively promoting visible-light photocatalysis, Adv. Mater. 22 (2010) 3317–3321.

[61] J. Li, W.H. Zhao, J. Wang, S.X. Song, X.Y. Wu, G.K. Zhang, Noble metal-free modified ultrathin carbon nitride with promoted molecular oxygen activation for photocatalytic formaldehyde oxidization and DFT study, Appl. Surf. Sci. 485 (2018) 59–69.

[62] K. Wang, X.Y. Wu, G.K. Zhang, J. Li, Y. Li, Ba$_5$Ta$_4$O$_{15}$ nanosheet/AgVO$_3$ nanoribbon heterojunctions with enhanced photocatalytic oxidation performance: Hole dominated charge transfer path and plasmonic effect insight, ACS Sustain. Chem. Eng. 6 (2018) 6682–6692.

[63] L. Wu, Y.Y. Xu, J.W. Zhang, D.Q. Zhang, G.S. Li, H.X. Li, Plasmon-induced photoelectrocatalytic activity of Au nanoparticles enhanced TiO$_2$ nanotube arrays electrodes for environmental remediation, Appl. Catal. B: Environ. 164 (2013) 217–224.

[64] D. Li, W.B. Cai, Y.G. Wang, Y.F. Zhu, Constructing a novel Bi$_2$SiO$_5$/BiPO$_4$ heterostructure with extended light response range and enhanced photocatalytic performance, Appl. Catal. B: Environ. 236 (2013) 205–211.

[65] J. Li, X.Y. Wu, W.F. Pan, G.K. Zhang, H. Chen, Vacancy-rich monolayer BiO$_{2-x}$ as a highly efficient UV, visible, and near-infrared responsive photocatalyst, Angew. Chem. Int. Ed. 57 (2018) 491–495.

[66] K. Wang, Y. Li, G.K. Zhang, J. Li, X.Y. Wu, 0D Bi nanodots/2D Bi$_3$NbO$_7$ nanosheets heterojunctions for efficient visible light photocatalytic degradation of antibiotics: Enhanced molecular oxygen activation and mechanism insight, Appl. Catal. B: Environ. 240 (2019) 39–49.

[67] Y.H. Liang, R. Shang, J.R. Lu, L. Liu, J.S. Hu, W.Q. Cui, Ag$_3$PO$_4$@UMOFNs core-shell structure: two-dimensional MOFs promoted photoinduced charge separation and photocatalysis, ACS Appl. Mater. Interfaces 10 (2018) 8758–8769.

[68] F.Y. Chen, W.J. An, L. Liu, Y.H. Liang, W.Q. Cui, Highly efficient removal of bisphenol A by a three-dimensional graphene hydrogel-AgBr@rGO exhibiting adsorption/photocatalysis synergy, Appl. Catal. B: Environ. 217 (2017) 65–80.

[69] W.Q. Cui, J. He, H. Wang, J.S. Hu, L. Liu, Y.H. Liang, Polyaniline hybridization promotes photo-electro-catalytic removal of organic contaminants over 3D network structure of rGH-PANI/TiO$_2$ hydrogel, Appl. Catal. B: Environ. 232 (2018) 232–245.

[70] B. Sun, D. Li, W.S. Linghu, X.H. Guan, Degradation of ciprofloxacin by manganese (III) intermediate: insight into the potential application of permanganate/bisulfite process, Chem. Eng. J. 339 (2018) 144–152.

[71] X.Y. Feng, P.F. Wang, J. Hou, J. Qian, Y.H. Ao, C. Wang, Significantly enhanced visible light photocatalytic efficiency of phosphorus doped TiO$_2$ with surface oxygen vacancies for ciprofloxacin degradation: synergistic effect and intermediates analysis, J. Hazard. Mater. 351 (2018) 196–205.

[72] H.B. Yu, B.B. Huang, H. Wang, X.Z. Yuan, L.B. Jiang, Z.B. Wu, J. Zhang, G.M. Zeng, Facile construction of novel direct solid-state Z-scheme AgI/BiOBr photocatalysts for highly effective removal of ciprofloxacin under visible light exposure: mineralization efficiency and mechanisms, J. Colloid Interface Sci. 522 (2018) 82–94.